Title (<120 characters): Measuring Compound Eye Optics with Microscope and MicroCT Images

Article Type: Tools and Resources

Author Names and Affiliations: John Paul Currea[1], Yash Sondhi[2], Akito Y. Kawahara[3], and Jamie Theobald[2]

[1]Department of Psychology, Florida International University, Miami, FL 33199, U.S.A.

[2]Department of Biological Sciences, Florida International University, Miami, FL 33199, U.S.A.

[3]Florida Museum of Natural History, University of Florida, Gainesville, FL, 32611, U.S.A.

Abstract (<150 words):

The arthropod compound eye is the most prevalent eye type in the animal kingdom, with an impressive range of shapes and sizes. Studying its natural range of morphologies provides insight into visual ecology, development, and evolution. In contrast to the camera-type eyes we possess, external structures of compound eyes often reveal resolution, sensitivity, and field of view if the eye is spherical. Non-spherical eyes, however, require measuring internal structures using imaging technology like MicroCT (µCT). Thus far, there is no efficient tool to automate characterizing compound eye optics. We present two open-source programs: (1) the ommatidia detecting algorithm (ODA), which automatically measures ommatidia count and diameter, and (2) a µCT pipeline, which calculates anatomical acuity, sensitivity, and field of view across the eye by applying the ODA. We validate these algorithms on images, images of replicas, and µCT scans from eyes of ants, fruit flies, moths, and a bee.

There are about 1.3 million described arthropod species, representing about 80% of described animal species (Zhang 2013). These arthropod species range vastly in size, lifestyle, and the habitat that they live in. With body lengths ranging from the 85 µm ectoparasitic crustacean *Tantulacus dieteri* (Mohrbeck, Arbizu, and Glatzel 2010) to the 0.5 m green rock lobster, *Sagmariasus verreauxi* (Holthuis 1991; Kensler 1967), arthropods inhabit nearly every ecological niche. Along with their diversity in body size and ecology is an array of eye architectures, the most common type being the compound eye (Cronin et al. 2014; Land and Nilsson 2012). In addition, recent progress in understanding compound eye development facilitates studying the selective pressures placed on the development of the compound eye (Casares and McGregor 2020; Currea, Smith, and Theobald 2018; Friedrich 2003; Gaspar et al. 2019; Harzsch and Hafner 2006). Because the compound eye found among arthropods is the most prevalent eye type in the animal kingdom and includes an array of morphologies that emerge following a relatively well-understood development, it is a prime subject in the study of vision (Cronin et al. 2014; Land and Nilsson 2012).

Studying eye morphology is fundamental to understanding how animals see because eye structure physically limits visual capacity (Land and Nilsson 2012). Depending on available light and image motion, an optimal eye architecture exists to maximize the ability to differentiate brightness levels and resolve spatial details (Land 1997; Snyder, Laughlin, and Stavenga 1977; Snyder, Stavenga, and Laughlin 1977). Because of the critical role of eye morphology in vision, studying the natural diversity of compound eye morphologies provides insight into visual ecology, development, and evolution. We offer two open-source programs written in Python to support the effort of characterizing compound eyes: (1) the ommatidia detecting algorithm (ODA), which automatically detects the individual facets, called ommatidia, in 2D images, and (2) a multi-stage µCT pipeline, which applies the ODA to segment individual crystalline cones and characterize the visual field.

In contrast to the camera-type eyes we possess, many structures that limit optical quality in compound eyes are externally visible. For example, a compound eye is composed of many individual units called ommatidia, each of which has a lens and a crystalline cone that direct light onto photoreceptors below. Ommatidia usually represent the individual pixels of an image, so their number limits the total number of images the eye can form, or its spatial information capacity, and they can be counted in microscope images. They range from ~20 ommatidia in one of the smallest flying insects, the fairyfly *Kikiki huna* (body length=158µm; Huber and Beardsley 2000; Huber and Noyes 2013) to >30,000 in large dragonflies, which have enhanced vision for hunting prey (Cronin et al. 2014).

In each ommatidium, the size of the lens restricts its aperture, which then limits the ability to discern luminance levels. High optical sensitivity is important for animals when photons are limited, such as under dim light or fast image motion (Snyder, Laughlin, et al. 1977; Snyder, Stavenga, et al. 1977; Theobald 2017; Warrant 1999). Compound eyes can be divided into two structural groups, apposition and superposition eyes. In apposition eyes, light from each ommatidium is separated by light-absorbing pigment cells and is restricted to a single rhabdom, such that lens size directly limits their optical sensitivity (Figure 1A). In superposition eyes, light is directed through a clear zone, so that many facets contribute to each point in the image (Figure 1B), thereby multiplying the final optical sensitivity (although still subject to the diffraction limit of the individual apertures).

Thus far, there has been little effort to develop tools and workflows to calculate ommatidia count and diameter, even though they can be derived from 2D images. Several algorithms and software plugins have been proposed to help extract ommatidia but require user input for each image and underestimate ommatidia counts (Woodman, Todd, and Staveley 2011), overestimate ommatidial diameter (Schramm et al. 2015), or were not validated against manual measurements or measurements in the literature (Diez-Hermano et al. 2015; Iyer et al. 2016; Vanhoutte, Michielsen, and Stavenga 2003). In addition, none of the programs were tested on more than one species, over a substantial range of eye sizes, or on different media. To support this effort, we offer an open-source program written in Python called the Ommatidia Detecting Algorithm (ODA). We test the reliability and validity of this technique on single images of 6 eye molds of 5 different ant species ranging dramatically in size, microscope images of 39 fruit flies (*Drosophila melanogaster*), and processed images of MicroCT (µCT) scans of 2 moths (*Manduca sexta* and *Deilephila elpenor*) and one bee (*Bombus terrestris*). The method is widely accessible because it only requires microscope imaging.

For spherical eyes, the lens diameter measurement provided by the ODA can be combined with measurements of eye radius (using the luminous pseudopupil technique, for instance) to measure the angular separation of ommatidia, called the interommatidial angle (IO angle; Figure 1 $\Delta\varphi$). The IO angle inversely limits spatial acuity or resolution (Land 1997; Snyder, Laughlin, et al. 1977; Snyder, Stavenga, et al. 1977). High spatial acuity affords many behaviors, such as prey, predator, and mate detection, and perceiving small changes in self-motion (Land 1997; Land and Nilsson 2012). For spherical eyes, the IO angle is approximately: $\Delta\varphi = D/R$, where D is the ommatidial lens diameter and R is the radius of curvature, assuming the axes of all ommatidia converge to a central point. Because of the limits imposed by photon noise and diffraction, smaller eyes face increasing constraints on IO angle and ommatidial size (Snyder, Stavenga, et al. 1977), generally resulting in homogeneous, spherical eyes. Likewise, because optical superposition eyes form an image by superposing light from many ommatidia on the retina below (Figure 1B), they often require a roughly spherical design (Land and Nilsson 2012). Thus, many compound eyes are safely approximated by the spherical model.

However, many compound eyes are non-spherical, having ommatidial axes askew to the eye surface. Skewed ommatidia sacrifice sensitivity by reducing their effective aperture as a function of the skewness angle and refraction. Further, skewness can improve acuity at the expense of field of view (FOV) by directing more ommatidia over a small visual field, decreasing the effective IO angle (Figure 1C). Alternatively, skewness can increase FOV at the expense of acuity by spreading a few ommatidia over a large visual field (Figure 1D).

MicroCT (µCT) is a 3D X-Ray imaging technique that provides a rich and valuable resource to study arthropod vision. Thus far, it has been used on arthropods to study muscles (Walker et al. 2014), brains (Smith et al. 2016), ocelli (Taylor et al. 2016), and eyes (Brodrick et al. 2020; Gaspar et al. 2019; Taylor et al. 2018, 2020). By visualizing internal structures in 3D, µCT affords calculating visual parameters for non-spherical compound eyes, measuring anatomical IO angles at very high spatial resolution, and segmenting different tissues, such as visual neuropils, within the same dataset.

Our second proposed method, the µCT pipeline, extracts crystalline cones from a µCT image stack (using the ODA) to measure the size, orientation, and spatial distribution of ommatidia. As mentioned

above, we validate it on µCT scans of the spherical eyes of two moth species (*M. sexta* and *D. elpenor*) collected by us and an open access scan of a non-spherical, oval bumblebee eye (*B. terrestris*) used in Taylor et al. (2018). For the bumblebee eye, we further demonstrate how the µCT pipeline can test for features of an oval eye; measure regional changes in skewness, spatial acuity, and sensitivity; and project onto world-referenced coordinates to more accurately measure FOV.

Because there are so many arthropod species and compound eye morphologies, it is challenging but valuable to characterize them in a meaningful, fast manner. Our proposed methods minimize the substantial labor that is typically required in characterizing optical performance in compound eyes and therefore facilitate understanding their role in visual ecology, development, and evolution.

Methods

Microscope Images

Eye Molds: Ants

Microscope images of eye molds or replicas were taken previously on five ant species. These species were: *Notoncus ectatommoides* (N=2 images) and a Golden tail sugar ant (*Camponotus aeneopilosus*) of the Formicinae subfamily, a jumper ant (*Myrmecia nigrocincta*) and a bull ant (*M. tarsata*) of the Myrmeciinae subfamily, and *Rhytidoponera inornata* of the Ectatomminae subfamily. Images of the first two species were obtained from Palavalli-Nettimi and Narendra (2018) and the latter three from Palavalli-Nettimi et al. (2019). Manual measurements of ommatidial counts and diameters were taken from their respective articles to compare with our automated measurements.

Direct Images: Fruit Flies

Microscope images of the eye of 39 fruit flies (*Drosophila melanogaster*) were obtained from the study of Currea et al. (2018). Ommatidial counts and diameters were measured by hand and compared to our automated measurements. Ommatidia were counted individually and diameters were measured as the average of 9 different sets of 9 sequential diameters around the center of the eye. Three sets were measured for each of the three major axes of the ommatidial array.

µCT

Moths

Micro-computed tomographs (µCTs) of two moth species, the tobacco hornworm (*Manduca sexta*) and the elephant hawkmoth (*Deilephila elpenor*), were collected. Vouchered specimens from the Florida Natural History Museum collections were stored in -20°C in 95% ethanol. Heads were sliced using sterilized scalpels and left to soak in the staining solution in Eppendorf vials or falcon tubes. The antennae were removed to allow for better stain penetration. Specimens were subjected to I2+KI (created by mixing in equal proportions 1.25% I2 and 2.5% KI solutions) staining to increase soft tissue contrast for 48–36 hours.

A fixed X-ray source was used to capture µCTs of the moth heads. The heads were placed in between the x-ray source and a detector and were rotated by small angles to get a complete 360 degree view of the sample. This generates a 3D X-ray image. Since Iodine is a heavy element, X-rays are absorbed depending on the amount of stain a portion of the sample has absorbed, creating differences in intensity in the final image stack.

The *Manduca sexta* specimen was scanned using a Phoenix V|Tome|X M system with a 180kv X-ray tube containing a diamond-tungsten target, with a tube voltage 80 kV and current of 110 µA, a source object distance of 17.8 mm and an object-detector distance of 793 mm and detector capture time adjusted for each scan to maximize absorption range for the specimen. The acquisition consisted of 2300 projections of 8 sec each. Raw x-ray data were processed using GE’s proprietary datos|x r software version 2.3 to produce a series of tomogram images and volumes, with final voxel resolution

of 4.50074 µm. The resulting µCT volume files were imported into VG StudioMax version 3.3.3 (Volume Graphics, Heidelberg, Germany), the eyes isolated using VG StudioMax's suite of segmentation tools, and then exported as cleaned Tiff stacks.

The *Deilephila elpenor* specimen was scanned using a Zeiss Xradia 520 Versa (Carl Zeiss Microscopy GmbH, Jena, Germany) using X-ray µCT, with a tube voltage 80 kV and current of 88 µA filtering of the low energy (the filter composition and thickness is not disclosed by the manufacturer); a source object distance of 22.5 mm and a object-detector distance of 210 mm; an indirect detector comprising a scintillator, a 0.392x optical lens and a charge-coupled device camera. The acquisition was performed using the software Scout-and-Scan (Carl Zeiss Microscopy GmbH), and consisted of 3201 projections of 8 sec each and using the adaptive motion correction option. The tomographic reconstruction was performed automatically generating a 32-bit txrm set of tomograms with an isotropic voxel size of 3.3250 µm. Finally, the data were converted to a stack of 16-bit tiff file using the XRM controller software (Carl Zeiss Microscopy GmbH).

Bumblebee

A bumblebee (*Bombus terrestris*) eye was scanned previously using a synchrotron X-ray source. CT imaging using a synchrotron source uses phase contrast in the samples between two slightly shifted X-ray beams to identify the different densities present in a sample (Baird and Taylor 2017). This scan was used with the permission of the author and it and other scans are available at https://www.morphosource.org/Detail/ProjectDetail/Show/project_id/646. See Taylor et al., (2018) for the details on the scans and specimens.

Ommatidia Detecting Algorithm (ODA)

The 2D Fast Fourier Transform (FFT) allows for the detection of 2D periodic patterns

The Fourier transform decomposes a function into a set of sinusoidal functions, each with its own frequency, amplitude, and phase, allowing detection of periodic patterns. The sinusoidal elements of a 2D Fourier transform are called gratings, and have an additional parameter of orientation, the angle perpendicular to the grating's wavefront. For digital images, the 2D Fast Fourier Transform (FFT) generates a 2D array of the same size, containing the component gratings, represented by their contrast, frequency, phase, and orientation (Figure 2 A).

Because the FFT is invertible, operations can be applied to the frequency representation, called the reciprocal space, then inverse transformed to generate a frequency filtered version of the original image. In particular, if we want to target a periodic, grating-like pattern in a picture, we can filter the relevant range of the spatial frequencies in the reciprocal space to amplify that pattern.

Ommatidia centers can be detected via a low-pass filter

The typical hexagonal arrangement of ommatidia has 3 major axes (Figure 2B blue, green and red). Each axis is approximated by a grating in the reciprocal space. By filtering out frequencies significantly higher than the three fundamental gratings, we can amplify the contribution of these ommatidial axes. The inverse FFT generates a smooth version of the original image, with peaks at the

approximate center of each ommatidium. Ommatidia centers are found near the local maxima of this inverse FFT image by using a local maxima detection algorithm.

ODA Python Module

A module written in Python was developed to apply the algorithm described above. A single image can be imported and processed through the ODA: (1) 2D FFT the image, (2) find the three fundamental gratings as local maxima closest to the center of the reciprocal image, (3) pass frequencies lower than those of the fundamental gratings, (4) inverse 2D FFT the filtered reciprocal space, and (5) find local maxima in the now smoothed image (Figure 2 B). Optionally, the user can view the generated reciprocal image with the local maxima superimposed to check that the program worked appropriately. The program stores a list of ommatidia coordinates in the image and calculates an average ommatidial diameter as the average distance between neighboring coordinates around the center of the image. Optionally, a binary mask (saved as a white silhouette on a black background) can be imported to avoid counting false positives outside of the eye. This program is available at www.github.com/jpcurrea/fly_eye/, where you can download the Python package and find some basic examples on how to use it.

Measuring Ommatidia using µCT

The ODA was applied to a pipeline for processing 3D, specifically µCT, data. Here we describe the fundamental elements of this pipeline.This program is available at www.github.com/jpcurrea/compound_eye_tools/, where you can download the Python package and find some basic examples on how to use it.

A. Import Stack

First, the large 3D dataset is reduced to coordinates found predominantly in the crystalline cones (Figure 3 A). These filtered coordinates should be saved as a stack of images to be imported by our program. Our program allows one to pre-filter data by choosing a range of density values in a graphical user interface, ideally isolating the crystalline cones but often including other structures. These images can be imported into an image editing program like ImageJ (Schneider, Rasband, and Eliceiri 2012) to clean up the individual slides, deleting irrelevant pixels. Once imported, our program allows a preview of the whole dataset (Figure 4 A).

B. Get Cross-Sectional Shells

Next, the coordinates are projected onto 2D images that can be processed through the ODA (Figure 3 B). Our program leverages the fact that the layer of crystalline cones is approximately a curved surface with little variation normal to the surface of the eye. A best-fitting sphere is found for the whole dataset using ordinary least squares regression and the sphere's center is saved. Then, the coordinates are transformed into spherical coordinates in reference to the sphere's center, representing each point by its radius, elevation, and azimuth.

In spherical coordinates, a continuous surface is fitted to the whole dataset, using linear interpolation to model the points' radii as a function of their elevation and azimuthal angles. With this fitted surface,

the coordinates are partitioned into two shells of points: those inside of the fitted surface (radii < surface radii) and those outside the surface (radii >= surface radii).

C. Find Ommatidial Clusters

Next, an image of each shell is formed by ignoring differences in radii and taking a 2D histogram of the coordinates' elevation and azimuth (Figure 3 C). However, to avoid extreme spherical warping, the coordinates are processed in 90°x 90° segments, each recentered before forming the histogram image. The ODA is applied to each segment, determining the approximate center of each lens within that segment. Then all of the centers are recombined onto the original spherical coordinate system by finding the nearest groups of points between each shell. Finally, each point in the dataset is labeled by its nearest center in each shell. By applying these labels to the original rectangular coordinates, the dataset has been effectively segmented into clusters of points representing separate crystalline cones.

Skewed Ommatidia

Steps B and C work for spherical eyes but fail if ommatidia are substantially skewed. For instance, if ommatidia are skewed by 45°, the offset between inside and outside shells can conflict with our ability to match points from the same cluster. When a cluster in one shell fails to find a pair in the other shell within a reasonable distance, that cluster is excluded from the count. To account for this, our program has an option specifically for non-spherical ommatidia. Instead of the two shells in step B, we extract one shell of points around the fitted surface containing 50% of the residuals (Figure 4 B). Then, as in step C, we partition the eye into 90° x 90° segments and find the centers of the clusters within this shell by applying the ommatidia finding algorithm to 2D histograms of the polar angles (Figure 4 C *top* and *middle*). We use the number of ommatidia from the algorithm to apply the spectral clustering algorithm to the total collection of points (Figure 4 C *bottom*). This method was successful for our bumblebee eye but was prohibitively time consuming on the larger moth scans.

D. Measure Visual Parameters

The number of clusters approximates the ommatidia count, which limits the total number of images the eye can form or its spatial information capacity. However, consider the number of ommatidial clusters at various stages of the pipeline. The initial count occurs at the beginning of step C, when applying the ODA, but is reduced if it fails to match the clusters of both shells for spherical eyes or if the clusters fail to be detected by the clustering algorithm for non-spherical eyes. Determining which count to use depends on the quality and resolution of the scan and can be settled by visual inspection of the cluster centers superimposed on the shells' 2D histograms.

The average distance between adjacent cluster centroids approximates the ommatidial lens diameter, which ultimately limits the eye's sensitivity, or ability to discern luminance levels. The ideal ommatidial axis is derived from the planes formed by triplets of centers near the cluster. By averaging the normal vector for each plane, we can approximate the vector orthogonal to the surface of the eye at each cluster. The anatomical ommatidial axis is derived by using singular value decomposition to find the longest semi-axis of the ellipsoid formed by the cluster. By finding the angular difference between the ideal and anatomical axes, we can measure the anatomical skewness of each ommatidium.

Ideally, the anatomical IO angles would be derived from the anatomical axes of neighboring ommatidia. However, such results were highly variable, especially in the bee scan (for instance, many of the resulting angles were negative). This was likely because the length of each cluster is small compared to the distance to the point of intersection, so that angular deviations in either axis have magnified effects on their intersection and thus interior angle. Getting such measurements to work might require increasing the resolution of the scan or using other structures, like the rhabdom, to extend our axis approximations closer to the intersection point.

Instead, anatomical IO angles are approximated by partitioning the coordinates into evenly spaced vertical and horizontal sections (Figure 4 D). For each section, all clusters within that section are projected onto a parallel plane. For instance, for vertical sections, all clusters within a range of x values are considered and the 2D clusters formed by their y and z values are used to determine their vertical IO angle component.

Then, the angle of the projected ommatidial axes are modeled as a function of their position, using nonlinear least squares regression. The program fits a polynomial function of degree between 2 and 5, only accepting a higher degree if it reduces the sum of the squared residuals by at least 5%. The function is constrained to having a positive first derivative, based on the assumption that the IO angles were never negative. This is repeated independently for each of the vertical and horizontal sections.

Once finished, the process approximates a horizontal and vertical angle for each cluster pair and we calculate the total angle as their hypotenuse. We call this hypotenuse the anatomical IO angle. While this method assumes one regression function per section, it allows for different regression models per section and independent approximations for horizontal and vertical IO angles across the eye (Stavenga 1979). In addition, by keeping track of the orientation of the cluster pairs along the surface of the eye, we can calculate the IO angles from horizontal and vertical IO angles using the two-dimensional lattice proposed by Stavenga (1979; Figure 6C).

Finally, two spreadsheets are saved: (1) for each crystalline cone cluster, the Cartesian and spherical coordinates of the centroid, the number and location of the points within its cluster, the approximate lens diameter, and the ideal and anatomical axis direction vectors are saved per row; and (2) for each pair of adjacent crystalline cones, the cones' indexes from spreadsheet 1, the center coordinates for the two cones, the resulting orientation in polar coordinates, and the anatomical IO angle between the two are saved per row. With these metrics, researchers can approximate how spatial acuity, optical sensitivity, and the eye parameter (Snyder 1979) vary across the eye (Taylor et al. 2018).

Results

Microscope Images

Eye Molds: Ants

We tested the ODA on images of flattened eye molds of six ants from 5 different species (Figure 5A). Ommatidia number and lens diameter measurements from the algorithm compared well to those taken manually on the same images. The automated counts were on average 97% (95.6 – 98.7%) of those taken by hand and they shared a strong and significant correlation ($r=.99$, $df=4$, $p \ll .0001$). The automated lens diameters were on average 99% (92.1 – 106.7%) of those taken by hand and they also shared a strong and significant correlation ($r=.82$, $df=4$, $p=.02$).

Direct Images: Fruit Flies

We also tested the ODA on microscope images of the eyes of 39 fruit flies (*D. melanogaster*; Figure 5B and C), validating the algorithm's performance on direct images of compound eyes and comparisons within a species. Ommatidia counts from the algorithm compared well to those taken manually on the same images. Automated counts shared a strong and significant correlation with manual counts ($r=.93$, $df=37$, $p \ll .0001$). Automated counts were 845±87 (mean±standard deviation) while hand counts were 810±76, with automated counts equalling 104±4% of those taken by hand. Though the difference in counts was not significant ($t=1.8$, $df=37$, $p=0.07$), automated counts may exceed the hand counts because of partial ommatidia that were excluded during the manual counting process but not the algorithm.

Lens diameter measurements from the algorithm also compared well to those taken manually on the same images. Automated diameters shared a strong and significant correlation with manual diameters ($r=.82$, $df=37$, $p \ll .0001$). Automated diameters were 16.3±1µm while manual diameters were 15.6±.8µm, with automated diameters equaling 105±3% of those taken by hand and is close to the 16µm taken previously (Franceschini 1972). Automatic diameters were greater than manual diameters ($t=4$, $df=37$, $p<.001$) possibly because manual diameters were calculated by taking the average over multiple sequences of ommatidia. This assumed the ommatidia centers are arranged in perfectly straight rows, though they curve slightly due to the curvature of the eye and can be interrupted by lattice abnormalities (Ready, Hanson, and Benzer 1976). By measuring individual diameters, the automatic diameters can account for irregularities in the ommatidial lattice and should equal at least those taken by averaging over a straight distance.

µCT

We tested our µCT pipeline on scans of compound eyes of two moth species (*M. sexta* and *D. elpenor*) collected by us and an publicly available scan of a bumblebee (*B. terrestris*) used in Taylor et al. (2018; Figure 7). The resulting measurements can be found in the table of Figure 7B. In addition, we tested methods specifically for non-spherical eyes on the bumblebee scan (Figure 8), including testing for features of an oval eye, measuring regional changes in aperture and anatomical IO angle, and projecting onto world-referenced coordinates.

Manduca sexta

We found that the *M. sexta* eye was composed of 27,756 ommatidia initially (µCT pipeline step B) but the dataset was reduced to 25,159 after later processing (step C). Visual inspection suggested that the first count is more accurate because the stack images were thoroughly cleaned before processing. The two counts are 103% and 93% of the previous approximation of 27,000 (White 2003) and 108% and 98% of the previous count of 25,641 taken on the same species (Stöckl, O'Carroll, and Warrant 2017). These ommatidia had lens diameters of 32.5±1.5µm, which is within range of previous measurements on the same species: 30µm (White 2003), 31µm (Stöckl et al. 2017), and 34µm (Theobald, Warrant, and O'Carroll 2010). The ommatidial axes were skewed by absolute angles of 5.7±4.4° (median±interquartile range), which are minor deviations potentially due to error in estimating the ommatidial axes or deformations of the eye during the µCT preparation procedure. We can calculate the minimum effect of this skewness on lens diameter by multiplying by the cosine of the skew angle, though the true angle is further skewed by refraction of the image space (Stavenga 1979). The adjustment without accounting for refraction resulted in a reduction of 0.16±.25µm or 0.5±.8%, which is minimal and consistent with a spherical eye. The ommatidia were separated by an anatomical IO angle of 0.94±.33°, which is close to our spherical approximation of .88±.16° and within the range of previous measurements of 0.91° (Stöckl et al. 2017) and 0.96° (Theobald et al. 2010) on the same species.

Deilephila elpenor

We found that the *D. elpenor* eye was composed of 13,801 ommatidia initially (step B) but the dataset was reduced to 12,172 after later processing (step C). Visual inspection suggests that there are substantial false positives in the first count because of noise around the boundary of the eye that we failed to remove in pre-processing. The two counts are 120% and 106% of the count of the previous approximation of 11,508 on the same species (Stöckl et al. 2017). These ommatidia had lens diameters of 28.8±1.9µm (mean±s.d.), which is consistent with previous measurements of 28µm (Stöckl et al. 2017) and 29µm (Johnsen 2006; Theobald et al. 2010) on the same species. The ommatidial axes were skewed by an absolute angle of 6.6±5.1° (median±IQR). The effect of this skewness on effective lens diameter was a reduction of .19±.31µm or .7±.11%, which again is minimal and consistent with a spherical eye. The ommatidia were separated by an anatomical IO angle of 1.49±0.74°, which is close to the spherical approximation of 1.27±0.35° and previous measurements of 1.12° (Stöckl et al. 2017) and 1.31° (Theobald et al. 2010) on the same species.

Bombus terrestris

We found that the *B. terrestris* worker bee eye was composed of 4,765 ommatidia initially (step B) but the dataset was reduced to 3,562 after later processing (step C*). Visual inspection of the 2D histograms and the superimposed ommatidial centers suggested that the first count is more accurate than the second, though it missed many ommatidia. The large hole in the eye map of Figures 4 and 6 is mostly due to differential exposure across the eye, resulting in many crystalline cones that were excluded at the pre-filter stage. The two counts are 85% and 64% of the 5,597 density-based count of the same scan (Taylor et al. 2018), and 85% of the previous count of 5,624±369 (mean±s.d.) for

conspecific worker bees counted manually (Streinzer and Spaethe 2014).

Despite missing a substantial number of ommatidia, our program provided some valid insights. The ommatidia had an average lens diameter of 26.1±2.1µm (mean±s.d.), which is consistent with the previous manual measurement of 25.6±2.5µm on the same scan (Taylor et al. 2018) and 25.1±1.9µm for worker bees of the same species (Streinzer and Spaethe 2014). The ommatidial axes were skewed by an absolute angle of 29.2±18.0° (median±IQR), which is consistent with previous anatomical measurements of skewness angles up to 50° (Baumgärtner 1928). The effect of this skewness on adjusted lens diameter was a reduction of 3.30±3.92µm or 12.7±15.4%, which is substantial and consistent with a non-spherical eye. The ommatidia were separated by an anatomical IO angle of 2.29±1.65°, which is greater than the spherical approximation of 0.74±.27°, the previous measurement of 1.6±0.6° using orthogonal ommatidial axes on the same scan (Taylor et al. 2018), and the previous measurement of 1.9° using the pseudopupil technique on a similarly sized conspecific (Spaethe 2003).

World-Referenced Visual Field

Above we used spherical coordinates for the azimuth and elevation about a single center point (step B). For the bee eye, this mostly accounted for curvature along the vertical axis but vastly underestimated curvature along the horizontal axis. To get a better measurement of their visual field, we projected the ommatidial axes onto a sphere outside of the eye, much like the world-referenced projection of Taylor et al. (2018; Figure 7C). However, instead of using the center of the head as our center, we used the center found in step B, which is near but not exactly the center of the head. We also chose a radius of 10cm based on their visual fixation behavior (Wehner and Flatt 1977). This world-referenced visual field has a FOV of about 140° horizontally and 140° vertically, agreeing exactly with previous measurements on the same scan, which did not account for skewness (Taylor et al. 2018).

Horizontal and Vertical Spatial Resolution

The bee eye is a non-spherical, oval eye, in which ommatidial axes intersect at different points for horizontally and vertically oriented IO pairs (I_h and I_v in Figure 6C). Anatomical IO angles therefore should be separated into independent horizontal and vertical components ($\Delta\varphi_h$ and $\Delta\varphi_v$ in Figure 6C). To apply this lattice configuration we converted our measurements of horizontal and vertical subtended angles from Method 6.4 into $\Delta\varphi_h$ and $\Delta\varphi_v$ and tested the accuracy of this oval eye model. In particular, if the eye is oval, (1) the horizontal angle for horizontal IO pairs (0° orientation) equals $2\Delta\varphi_h$ while the vertical angle equals 0; (2) the horizontal and vertical angles for diagonal IO pairs (±60° orientations) are $\Delta\varphi_h$ and $\Delta\varphi_v$; and (3) the proportion $\Delta\varphi_v / \Delta\varphi_h$ should equal $1/\sqrt{3}$. (Stavenga 1979)

In our bee eye dataset, IO pair orientations followed a trimodal distribution with modes at -59°, 0°, and 61° (K Means algorithm with 3 means; N=11,626, mean distance=12°). We selected IO pairs within 15° of these centroids to more accurately measure the horizontal and vertical angles (Figure 7A). For horizontal pairs (orientation=0.0±15°), the horizontal subtended angle was 2.94±1.08° while the vertical angle was 0.08±.10° (N=2,675). For negative diagonal pairs (orientation=-59±15°), the horizontal angle was 1.90±.81° while the vertical angle was .97±0.50° (N=2,435). For positive diagonal pairs (orientation=61±15°), the horizontal angle was 1.36±0.60° while the vertical angle was .98±0.49° (N=2,393). As a result, our dataset fits several of the predictions of an oval eye: (1) the

horizontal angle for horizontal IO pairs, 2.94°, is nearly twice the horizontal angle for diagonal pairs, 1.90°+1.36°=3.26° while the vertical angle, 0.08°, is close to 0; and (2) the vertical angles for diagonal IO pairs, .97° and .98°, are nearly equal. However, the horizontal angles for diagonal IO pairs, 1.90° and 1.36°, which should be equal, differ by about 28%.

By combining the horizontal angle of diagonal pairs and half the horizontal angle of horizontal pairs, we approximate the horizontal anatomical IO angle component, $\Delta\varphi_h$=1.48±.88° (N=7,503). This is close to the range of 1.8°–3.3° measured previously (Spaethe 2003). By combining the vertical angles of diagonal pairs we approximate $\Delta\varphi_v$=.95±0.60° (N=4,828), which is within the range of 0.6°–1.4° measured in Spaethe (2003). Using these two anatomical IO angle components, the total anatomical IO angle $\Delta\varphi$= 1.76°, is closer to the previous measurements of 1.6° and 1.9° mentioned above. Also, the proportion $\Delta\varphi_v/\Delta\varphi_h$=.64 is close to $1/\sqrt{3}$=0.58, as predicted for an oval eye.

The anatomical IO angle components also varied as a function of elevation and azimuth angles (Figure 7B and C). To measure the change in these parameters with respect to azimuth and elevation, we binned values into 15° intervals. $\Delta\varphi_v$ decreases horizontally from a maximum of 1.1±0.33° at -37.5° azimuth (bin N=571) to a minimum of 0.80±1.02° at 7.5° azimuth (N=705), and then increases to a local maximum of .94±0.33° at 37.5° azimuth (N=614). This corresponds to a weak negative correlation (r=-.14, df=2174, $p \ll 0.0001$) from -37.5° to 7.5° azimuth followed by an insignificant positive correlation up to 37.5° (r=0.01, df=1,414, p=0.60; Figure B, top left). To our knowledge, this has not been measured previously but is consistent with the observation that the greatest overall acuity is in the central visual field (Baumgärtner 1928).

$\Delta\varphi_v$ decreases vertically from a maximum of 1.78±.74° at -67.5° elevation (N=53) to a minimum of 0.51±0.63° at 22.5° azimuth (N=1294), and then increases to a local maximum of 1.21±0.67° at 52.5° azimuth (N=57). This corresponds to a strong negative correlation (r=-0.53, df=4870, $p \ll 0.0001$) followed by a moderate positive correlation (r=0.29, df=2207, $p \ll 0.0001$; Figure B, top right). This agrees partially with previous measurements showing a decrease from about 2.4° ventrally to about 1° centrally followed by a gradual increase to about 2° dorsally. However, the previous measurement found a dramatic increase to 4° at the dorsal extreme (Baumgärtner 1928), which we did not measure. Differences in these measurements are likely due to technical differences: their bee species is unspecified and may differ from *B. terrestris* used here; their specific bee specimen may be smaller and thus have a larger $\Delta\varphi_v$ minimum than ours; and our eye scan lacks a substantial dorsal portion where they measured most of the increase in $\Delta\varphi_v$. (Baumgärtner 1928)

$\Delta\varphi_h$ decreases from a maximum of 2.23±2.25° at -67.5° azimuth (N=52) to a relatively constant range from 1.40±0.88° at -22.5° azimuth (N=1,178) to 1.55±0.82° at 52.5° azimuth (N=455). This actually corresponded to a weak negative correlation (r=-0.03, df=6295, p<0.01). This differs from the previous measurements taken on the same scan, which found that the anatomical IO angle increases from about 1.26° to 1.90° from the lateral to central eye with a strong positive correlation (r=0.50, df=3,471, $p \ll 0.0001$; Taylor et al., 2018). This is likely because the previous measurements did not account for skewness which we find increases laterally, explaining partially why our anatomical IO angle measurement exceeds theirs by about 0.16°.

Finally, $\Delta\varphi_h$ decreases vertically from a maximum of 2.07±1.11° at -52.5° elevation (N=274) to a minimum of 1.49±0.74° at 7.5° elevation (N=1,528), with an insignificant correlation (r=0.03, df=4,750, p=0.06; Figure 7B, bottom right).

Sensitivity, Acuity, and FOV Tradeoffs

Adjusted lens diameter also varied as a function of azimuth and elevation angle. Adjusted lens diameter increases horizontally from a minimum of 19.9±6.7µm at -37.5° azimuth (N=476) to a maximum of 24.1±3.1µm at 37.5° azimuth (N=430), with a moderate positive correlation (r=0.28, df=3,542, $p \ll 0.0001$; Figure 7B, bottom left, blue). This correlation is largely reduced for the absolute lens diameter (r=0.09, df=3,542, $p \ll 0.0001$; Figure 7B, bottom left, blue dashed line).

Adjusted lens diameter also increases vertically from a minimum of 18.5±4.0µm at -67.5° elevation (N=100) to a maximum of 23.7±3.9µm at 7.5° azimuth (N=559; Figure B, bottom left, blue). This corresponds to a moderate positive correlation below 7.5° elevation (r=0.25, df=1,845, $p \ll 0.0001$), which is completely reduced for the absolute lens diameter (r=-0.006, df=3,542, p=0.8; Figure 7B, top right, blue dashed line).

These positional changes in adjusted lens diameter and anatomical IO angle components reveal interesting tradeoffs between FOV, sensitivity, and the horizontal and vertical spatial acuities caused by skewness across the eye. As we stated in the introduction, skewness always reduces sensitivity but can lead to FOV and IO angle tradeoffs. In this case, adjusted lens diameter, and consequently sensitivity, increases from the lateral to central visual field while vertical spatial acuity first increases slightly until near the center and then decreases medially. Similarly, adjusted lens diameter, and consequently sensitivity, increases from the ventral to dorsal visual field while vertical spatial acuity also increases. This results in high sensitivity and vertical spatial acuity near the central visual field at the expense of FOV, and high FOV laterally and ventrally at the expense of sensitivity and vertical spatial acuity. Both of these effects are largely invisible based on absolute lens diameters or IO angles that do not account for skewness. Hence, the regional tradeoffs and specializations are due to ommatidial skewness. These same tradeoffs are found among many apposition eyes, though they usually coincide with visible changes in the curvature of the eye. These results highlight the flexibility gained by skewing ommatidia as well as their deceptive nature.

Skewness-Based Eye Regions

Skewness angle varied systematically across the bee eye (Figure 7C). In particular, there were 3 regions of generally different skewness angles (separated by the dashed white lines in Figure 7C): (1) small angles centrally and medial-dorsally (19±10°) and (2) moderate angles dorso-laterally (35±13°), and (3) ventrally (37±14°). This skewness resulted in 3 regions of generally different adjusted lens diameters: (1) larger diameters centrally and medially (24±3µm); (2) moderate diameters dorso-laterally (22±4µm); and (3) small diameters ventrally (20±5µm).

While $\Delta\varphi_h$ remained constant across these three regions ($\Delta\varphi_h$=[1.5±0.8°, 1.5±0.7°, 1.5±1.1°], N=[3048, 1626, 2765]), $\Delta\varphi_v$ varied. (1) The lowest vertical IO components, $\Delta\varphi_v$=0.81±0.52° (N=2,005), resulting in the lowest total anatomical IO angle, $\Delta\varphi$=1.7°, were in the medial-dorsal region of lowest skewness.

(2) The largest vertical IO angles, $\Delta\varphi_v$=1.3±0.7° (N=1,041), resulting in the largest total anatomical IO angle, $\Delta\varphi$=1.98°, were in the dorso-lateral region of moderate skewness. (3) Moderate vertical IO angles, $\Delta\varphi_v$=0.97±0.56° (N=1,740), resulting in the second lowest total anatomical IO angle, $\Delta\varphi$=1.75°, were in the ventral region of maximum skewness.

Although regions 2 and 3 have nearly the same amount of skewness, 35° and 37°, their anatomical IO angles, 1.98° and 1.75°, and thus spatial resolutions differ by about 12%. As we mentioned in the introduction, this is because skewness confers a trade-off between FOV and spatial acuity. As a result, the skewness in region 2 extends the FOV dorsally, while in region 3 it maintains a moderate spatial resolution.

Also, the region of minimal skewness, largest adjusted lens diameters, and smallest anatomical IO angles (region 1) coincides with two visual regions of ecological significance. First, during visual fixation, bees incline their dorsal-ventral axis to 70° (Wehner and Flatt 1977), adjusting our elevation parameter by -20°. Thus they direct the approximate center of this region (azimuth=0°, elevation=20°), which is near the maximum adjusted lens diameter and minimum anatomical IO angle, towards visual targets. Second, binocular overlap occurs in the dorsal part of this region (Taylor et al. 2018). As a result, the region involved in visual fixation and binocular overlap has the lowest average skewness and the highest sensitivity and acuity.

Discussion

The methods proposed here successfully automate the estimation of multiple visual parameters of compound eyes. We tested the ommatidia detecting algorithm (ODA), which filters spatial frequencies based on the hexagonal arrangement of the ommatidial lattice and applies a local maximum detector to identify the centers of ommatidia in images of compound eyes. We applied this algorithm to calculate the ommatidial lens diameter and count from different media (eye molds, microscope images, and µCT scans), taxa (ants, flies, moths, and a bee), sizes (hundreds to tens of thousands of ommatidia), and eye type (apposition, neural superposition, and optical superposition). In all cases, measurements provided by the program matched well with manual measurements on the same data, previous measurements in the literature, or both. Ommatidial counts were accurate, with an average proportion across all tested species of 93–102% (mean of low means – mean of high means%) of previous or manual measurements. Ommatidial diameters were even more accurate, with an average proportion across all tested species of 100.2–103.4% of previous or manual measurements.

Integrating the ODA into a larger µCT pipeline proved successful on scans of two spherical moth eyes (*D. elpenor* and *M. sexta*) and one oval bee eye (*B. terrestris*). In addition to ommatidia counts and lens diameters, the pipeline provided estimates of anatomical IO angles, FOV, and skewness. This offered the calculation of an adjusted lens diameter, approximating the aperture-diminishing effect of skewed ommatidia. As expected for spherical eyes, skewness angles were insignificant in the two moth eyes, which generally require spheracity for proper optical superposition. However, when applied to the oval eye of the bumblebee, there were significant skewness angles, implying a reduction in optical sensitivity. Again, the estimates provided were consistent with manual measurements on the same data, previous measurements in the literature, or both.

On the bumblebee eye, we demonstrated additional advantages of high resolution 3D data, world-referenced coordinates, and regional measurements across the visual field. These included the measurement of regional changes in skewness, vertical spatial acuity, and sensitivity as well as regional three-way tradeoffs between spatial acuity, FOV, and sensitivity caused by skewness. Though many of these insights were consistent with previous studies and measurements on the same scan, some were previously unknown.

One example reveals an unexpected advantage of using 3D data. Traditional methods of measuring IO angle facilitate measurements oriented along the same axis but make it challenging to measure IO angles oriented along a perpendicular axis. For example, when using histological sections, it is easier and more efficient to measure multiple IO angles parallel to the sectioning plane than to measure individual IO angles perpendicularly along many sections. With a 3D dataset, however, the two are equally difficult. As a result, across the bee eye we were able to measure horizontal resolution increasing vertically and vertical resolution increasing horizontally from the peripheral to the central visual field. As far as we know, this has not been measured previously though it is consistent with previous measurements showing the greatest resolution in the central visual field (Baumgärtner 1928).

In addition to the empirical benefits of our programs, they provide several technical advantages by design. First, they are both open source and easy to install. The ODA can be downloaded as a Python

module (https://github.com/jpcurrea/fly_eye) and we are in the process of adding several command-line tools for those who are not programming savvy. The µCT pipeline can also be downloaded as a Python module (https://github.com/jpcurrea/compound_eye_tools) with command-line and graphical user interfaces available to run on individual image stacks. Both have been designed in a modular fashion so that collaborators can easily incorporate portions of the library into other, custom pipelines. For instance, the pipeline can be easily customized to run on a computer cluster.

The two programs presented here have some limitations. First, the ODA requires images with sufficient resolution in order to properly detect ommatidia. For single images, this requires that the pixel length be at most half the smallest ommatidial diameter. For the µCT pipeline, this is ultimately affected by the resolution of the scan: if individual crystalline cones cannot be resolved at each layer, they are likely indiscriminable once fed into the ODA. Also, some species, preparations, and µCT scanning procedures appear better than others at capturing the contrast between crystalline cones and the other structures while avoiding structural damage to the specimen. For instance, crystalline cones in the *M. sexta* scan were prefiltered simply by using the threshold function because the crystalline cones contrasted sharply with the background. This was not the case for *D. elpenor*, which had additional noise outside of the eye, and *B. terrestris*. The *B. terrestris* scan had a particular problem with uneven exposure, resulting in different density measurements depending on the location in the scan and ultimately the omission of data. This may be an unintentional consequence of the contrast enhancing property of a synchrotron light source (Baird and Taylor 2017).

Ultimately, anatomical measurements cannot replace optical techniques in measuring compound eye optics (Stavenga 1979; Taylor et al. 2018). When light passes through the eye optics, the angle of refraction is determined by both the incident angle and the index of refraction of the image space (Stavenga 1979). In our approximations, however, we used only the incident angle. As a result, our measurements of the aperture-diminishing effect of skewness represent lower bounds and our program specifically provides measurements of *anatomical* IO angles as opposed to functional IO angles. Ultimately, though skewness can be somewhat corrected for, no methods are as accurate as optical techniques (Stavenga 1979).

Because of their great range of eye morphologies (Land and Nilsson 2012), and both inter- and intraspecific variation in size (Casares and McGregor 2020; Currea et al. 2018; Gaspar et al. 2019; Land 1997; Land and Nilsson 2012; Shingleton et al. 2007), compound eyes are ideal candidates for studying environmental reaction norms and allometry. Very little research on allometry has dealt with compound eyes, generally resorting to the allometry of organs that can be measured in one or two dimensions (McDonald et al. 2018; Shingleton et al. 2007; Shingleton, Mirth, and Bates 2008). Our programs automate the more tedious tasks of characterizing compound eyes and therefore should help with this challenge. For instance, ommatidia counts and diameters derived from the ODA allow for total cell count approximations and correspond to the independent effects of cellular proliferation and growth during eye development. Further, our program facilitates measuring the allometry of visual performance, allowing us to measure the environmental reaction norms of the anatomical determinants of vision.

Characterizing compound eye morphology also applies to research in visual development, plasticity,

neurobiology, and neuroethology. Thanks in large part to progress in understanding eye development in fruit flies (*D. melanogaster*; Callier and Nijhout 2013; Casares and McGregor 2020; Gaspar et al. 2019; Ready et al. 1976), compound eyes are ideal for assessing principles of eye development and how they may vary across different taxa (Casares and McGregor 2020; Friedrich 2003; Harzsch and Hafner 2006). Also, because eye optics are the first limit to incoming visual information (Land 1997; Stavenga 1979), they inform behavioral or electrophysiological data to infer intermediate neural processing (Currea et al. 2018; Gonzalez-Bellido, Wardill, and Juusola 2011; Juusola et al. 2017; Land and Nilsson 2012; Theobald et al. 2010; Wardill et al. 2017; Warrant 1999).

Conclusion

Arthropods are the most diverse eukaryotic phylum and occupy nearly every ecological niche on Earth. They possess the most common eye type, the compound eye, which varies dramatically in size, shape, and architecture across widely diverse visual environments. Because compound eyes are diverse, ubiquitous, and have undergone substantial natural selection, studying their natural range of morphologies and optical limitations is imperative to understanding the evolution and development of vision. Our programs successfully measure optical parameters of a wide range of compound eye shapes and sizes, minimizing labor and facilitating the study of the development, evolution, and ecology of visual systems in non-model organisms.

Despite the programs we present here, more work is needed to understand the limitations of both the ODA and the µCT pipeline. Because the ODA depends on passing the spatial frequencies corresponding inversely to the ommatidial diameter, an eye with a wide range of diameters may not work. The ODA should be tested on images of eyes with highly acute or sensitive zones, such as the robberfly (Wardill et al. 2017) and ommatidia lattices with regions of transitioning arrangements, such as the transition from hexagon to square in houseflies (Stavenga 1975) and male blowflies (Smith et al. 2015). Likewise, the µCT pipeline should be tested on non-spherical non-oval eyes. While our program appropriately measured anatomical IO angles across the bumblebee's oval eye and actually corroborated its oval eye properties, it may not work when IO angles change dramatically like in the robberfly (Wardill et al. 2017). Finally, the µCT pipeline should be tested on non-insect arthropods.

Funding: This research was supported by grants from the National Science Foundation: IOS-1750833 to JT, BCS-1525371 to JC, DEB-1557007 to AYK and JT and IOS-1920895 to AYK. The content is solely the responsibility of the authors and does not necessarily represent the official views of the National Institutes of Health or the National Science Foundation.

Acknowledgements: We thank members of the Kawahara Lab at the Florida Museum of Natural History, McGuire Center for Lepidoptera and Biodiversity, for raising and vouchering moth specimens. The University of Florida CT facility is thanked for helping acquiring the *M. sexta* CT scan, and Kelly Dexter for help with sample staining. We thank Deborah Glass and Ian Kitching from the Natural History Museum of London for help with the CT procedure and sharing the *D. elpenor* CT scan, which study was funded by NERC grant number NE/P003915/1 to IJK. Gavin Taylor and Emily Baird shared their CT scans of *B. terrestris*. Michael Reisser and Arthur Zhao provided valuable discussions

regarding the uCT pipeline.

References

Baird, Emily, and Gavin Taylor. 2017. “X-Ray Micro Computed-Tomography.” *Current Biology* 27(8):R289–91. doi: 10.1016/j.cub.2017.01.066.

Baumgärtner, Herbert. 1928. “Der Formensinn Und Die Sehschärfe Der Bienen.” *Zeitschrift Für Vergleichende Physiologie* 7(1):56–143.

Brodrick, Emelie A., Nicholas W. Roberts, Lauren Sumner Rooney, Christian M. Schlepütz, and Martin J. How. 2020. “Light Adaptation Mechanisms in the Eye of the Fiddler Crab *Afruca Tangeri*.” *Journal of Comparative Neurology* cne.24973. doi: 10.1002/cne.24973.

Callier, Viviane, and H. Frederik Nijhout. 2013. “Body Size Determination in Insects: A Review and Synthesis of Size- and Brain-Dependent and Independent Mechanisms.” *Biological Reviews* 88(4):944–54. doi: 10.1111/brv.12033.

Casares, Fernando, and Alistair P. McGregor. 2020. “The Evolution and Development of Eye Size in Flies.” *WIREs Developmental Biology* n/a(n/a):e380. doi: 10.1002/wdev.380.

Cronin, Thomas W., Sönke Johnsen, N. Justin Marshall, and Eric J. Warrant. 2014. *Visual Ecology*. Princeton University Press.

Currea, John P., Joshua L. Smith, and Jamie C. Theobald. 2018. “Small Fruit Flies Sacrifice Temporal Acuity to Maintain Contrast Sensitivity.” *Vision Research* 149:1–8. doi: 10.1016/j.visres.2018.05.007.

Diez-Hermano, Sergio, Jorge Valero, Cristina Rueda, Maria D. Ganfornina, and Diego Sanchez. 2015. “An Automated Image Analysis Method to Measure Regularity in Biological Patterns: A Case Study in a Drosophila Neurodegenerative Model.” *Molecular Neurodegeneration* 10(1):9. doi: 10.1186/s13024-015-0005-z.

Franceschini, N. 1972. “Pupil and Pseudopupil in the Compound Eye of Drosophila.” Pp. 75–82 in *Information Processing in the Visual Systems of Anthropods*, edited by R. Wehner. Berlin, Heidelberg: Springer Berlin Heidelberg.

Friedrich, Markus. 2003. “Evolution of Insect Eye Development: First Insights from Fruit Fly, Grasshopper and Flour Beetle.” *Integrative and Comparative Biology* 43(4):508–21. doi: 10.1093/icb/43.4.508.

Gaspar, Pedro, Saad Arif, Lauren Sumner-Rooney, Maike Kittelmann, David L. Stern, Maria D. S. Nunes, and Alistair P. McGregor. 2019. “Characterisation of the Genetic Architecture Underlying Eye Size Variation within Drosophila Melanogaster and Drosophila Simulans.” *BioRxiv* 555698. doi: 10.1101/555698.

Gonzalez-Bellido, Paloma T., Trevor J. Wardill, and Mikko Juusola. 2011. “Compound Eyes and Retinal Information Processing in Miniature Dipteran Species Match Their Specific Ecological Demands.” *Proceedings of the National Academy of Sciences* 108(10):4224–29. doi: 10.1073/pnas.1014438108.

Harzsch, Steffen, and Gary Hafner. 2006. “Evolution of Eye Development in Arthropods: Phylogenetic Aspects.” *Arthropod Structure & Development* 35(4):319–40. doi: 10.1016/j.asd.2006.08.009.

Holthuis, Lipke B. 1991. “Marine Species Identification Portal : Green Rock Lobster - Jasus Verreauxi.” *Food and Agriculture Organization of the United Nations* 13(125).

Huber, John, and John Noyes. 2013. “A New Genus and Species of Fairyfly, Tinkerbella Nana (Hymenoptera, Mymaridae), with Comments on Its Sister Genus Kikiki, and Discussion on Small Size Limits in Arthropods.” *Journal of Hymenoptera Research* 32:17–44. doi: 10.3897/jhr.32.4663.

Huber, John T., and John W. Beardsley. 2000. “A New Genus of Fairyfly, Kikiki, from the Hawaiian Islands (Hymenoptera: Mymaridae).” *Hawaiian Entomological Society*.

Iyer, Janani, Qingyu Wang, Thanh Le, Lucilla Pizzo, Sebastian Grönke, Surendra S. Ambegaokar, Yuzuru Imai, Ashutosh Srivastava, Beatriz Llamusí Troisí, and Graeme Mardon. 2016.

"Quantitative Assessment of Eye Phenotypes for Functional Genetic Studies Using Drosophila Melanogaster." *G3: Genes, Genomes, Genetics* 6(5):1427–1437.

Johnsen, S. 2006. "Crepuscular and Nocturnal Illumination and Its Effects on Color Perception by the Nocturnal Hawkmoth Deilephila Elpenor." *Journal of Experimental Biology* 209(5):789–800. doi: 10.1242/jeb.02053.

Juusola, Mikko, An Dau, Zhuoyi Song, Narendra Solanki, Diana Rien, David Jaciuch, Sidhartha Anil Dongre, Florence Blanchard, Gonzalo G. de Polavieja, Roger C. Hardie, and Jouni Takalo. 2017. "Microsaccadic Sampling of Moving Image Information Provides Drosophila Hyperacute Vision." *ELife* 6. doi: 10.7554/eLife.26117.

Kensler, Craig B. 1967. "The Distribution of Spiny Lobsters in New Zealand Waters (Crustacea: Decapoda: Palinuridae)." *New Zealand Journal of Marine and Freshwater Research* 1(4):412–20. doi: 10.1080/00288330.1967.9515216.

Land, Michael F. 1997. "Visual Acuity in Insects." *Annual Review of Entomology* 42(1):147–177.

Land, Michael F., and Dan-Eric Nilsson. 2012. *Animal Eyes*. OUP Oxford.

McDonald, Jeanne M. C., Shampa M. Ghosh, Samuel J. L. Gascoigne, and Alexander W. Shingleton. 2018. "Plasticity Through Canalization: The Contrasting Effect of Temperature on Trait Size and Growth in Drosophila." *Frontiers in Cell and Developmental Biology* 6:156. doi: 10.3389/fcell.2018.00156.

Mohrbeck, Inga, Pedro Martínez Arbizu, and Thomas Glatzel. 2010. "Tantulocarida (Crustacea) from the Southern Ocean Deep Sea, and the Description of Three New Species of Tantulacus Huys, Andersen & Kristensen, 1992." *Systematic Parasitology* 77(2):131–51. doi: 10.1007/s11230-010-9260-0.

Palavalli-Nettimi, Ravindra, and Ajay Narendra. 2018. "Miniaturisation Decreases Visual Navigational Competence in Ants." *Journal of Experimental Biology* 221(7):jeb177238.

Palavalli-Nettimi, Ravindra, Yuri Ogawa, Laura A. Ryan, Nathan S. Hart, and Ajay Narendra. 2019. "Miniaturisation Reduces Contrast Sensitivity and Spatial Resolving Power in Ants." *Journal of Experimental Biology* 222(12). doi: 10.1242/jeb.203018.

Ready, Donald F., Thomas E. Hanson, and Seymour Benzer. 1976. "Development of the Drosophila Retina, a Neurocrystalline Lattice." *Developmental Biology* 53(2):217–40. doi: 10.1016/0012-1606(76)90225-6.

Schneider, Caroline A., Wayne S. Rasband, and Kevin W. Eliceiri. 2012. "NIH Image to ImageJ: 25 Years of Image Analysis." *Nature Methods* 9(7):671–75.

Schramm, Bartosz W., Agnieszka Gudowska, Filip Kapustka, Anna Maria Labecka, Marcin Czarnoleski, and Jan Kozłowski. 2015. "Automated Measurement of Ommatidia in the Compound Eyes of Beetles." *BioTechniques* 59(2):99–101. doi: 10.2144/000114316.

Shingleton, Alexander W., W. Anthony Frankino, Thomas Flatt, H. Frederik Nijhout, and Douglas. J. Emlen. 2007. "Size and Shape: The Developmental Regulation of Static Allometry in Insects." *BioEssays* 29(6):536–48. doi: 10.1002/bies.20584.

Shingleton, Alexander W., Christen K. Mirth, and Peter W. Bates. 2008. "Developmental Model of Static Allometry in Holometabolous Insects." *Proceedings of the Royal Society of London B: Biological Sciences* 275(1645):1875–85. doi: 10.1098/rspb.2008.0227.

Smith, Dylan B., Galina Bernhardt, Nigel E. Raine, Richard L. Abel, Dan Sykes, Farah Ahmed, Inti Pedroso, and Richard J. Gill. 2016. "Exploring Miniature Insect Brains Using Micro-CT Scanning Techniques." *Scientific Reports* 6(1). doi: 10.1038/srep21768.

Smith, J. L., N. A. Palermo, J. C. Theobald, and J. D. Wells. 2015. "Body Size, Rather Than Male Eye Allometry, Explains Chrysomya Megacephala (Diptera: Calliphoridae) Activity in Low Light." *Journal of Insect Science* 15(1):133. doi: 10.1093/jisesa/iev114.

Snyder, Allan W. 1979. "Physics of Vision in Compound Eyes." Pp. 225–313 in *Comparative Physiology and Evolution of Vision in Invertebrates, Handbook of Sensory Physiology*, edited

by H. Autrum. Springer Berlin Heidelberg.
Snyder, Allan W., Simon B. Laughlin, and Doekele G. Stavenga. 1977. “Information Capacity of Eyes.” *Vision Research* 17(10):1163–75. doi: 10.1016/0042-6989(77)90151-1.
Snyder, Allan W., Doekele G. Stavenga, and Simon B. Laughlin. 1977. “Spatial Information Capacity of Compound Eyes.” *Journal of Comparative Physiology* 116(2):183–207.
Spaethe, J. 2003. “Interindividual Variation of Eye Optics and Single Object Resolution in Bumblebees.” *Journal of Experimental Biology* 206(19):3447–53. doi: 10.1242/jeb.00570.
Stavenga, Doekele G. 1975. “The Neural Superposition Eye and Its Optical Demands.” *Journal of Comparative Physiology ? A* 102(4):297–304. doi: 10.1007/BF01464342.
Stavenga, Doekele G. 1979. “Pseudopupils of Compound Eyes.” Pp. 357–439 in *Comparative Physiology and Evolution of Vision in Invertebrates*. Vol. 7 / 6 / 6 A, edited by H. Autrum. Berlin, Heidelberg: Springer Berlin Heidelberg.
Stöckl, A. L., D. O’Carroll, and E. J. Warrant. 2017. “Higher-Order Neural Processing Tunes Motion Neurons to Visual Ecology in Three Species of Hawkmoths.” *Proceedings of the Royal Society B: Biological Sciences* 284(1857):20170880. doi: 10.1098/rspb.2017.0880.
Streinzer, Martin, and Johannes Spaethe. 2014. “Functional Morphology of the Visual System and Mating Strategies in Bumblebees (Hymenoptera, Apidae, *Bombus*): *Bombus* Compound Eye Morphology.” *Zoological Journal of the Linnean Society* 170(4):735–47. doi: 10.1111/zoj.12117.
Taylor, Gavin J., Stephen A. Hall, Johan A. Gren, and Emily Baird. 2020. “Exploring the Visual World of Fossilized and Modern Fungus Gnat Eyes (Diptera: Keroplatidae) with X-Ray Microtomography.” *Journal of The Royal Society Interface* 17(163):20190750. doi: 10.1098/rsif.2019.0750.
Taylor, Gavin J., Willi Ribi, Martin Bech, Andrew J. Bodey, Christoph Rau, Axel Steuwer, Eric J. Warrant, and Emily Baird. 2016. “The Dual Function of Orchid Bee Ocelli as Revealed by X-Ray Microtomography.” *Current Biology* 26(10):1319–24. doi: 10.1016/j.cub.2016.03.038.
Taylor, Gavin J., Pierre Tichit, Marie D. Schmidt, Andrew J. Bodey, Christoph Rau, and Emily Baird. 2018. “Bumblebee Visual Allometry Results in Locally Improved Resolution and Globally Improved Sensitivity.” *BioRxiv*. doi: 10.1101/380527.
Theobald, Jamie. 2017. “Optic Flow Induces Spatial Filtering in Fruit Flies.” *Current Biology* 27(6):R212–R213.
Theobald, Jamie C., Eric J. Warrant, and David C. O’Carroll. 2010. “Wide-Field Motion Tuning in Nocturnal Hawkmoths.” *Proceedings of the Royal Society of London B: Biological Sciences* 277(1683):853–60. doi: 10.1098/rspb.2009.1677.
Vanhoutte, Kurt J. A., Kristel F. L. Michielsen, and Doekele G. Stavenga. 2003. “Analyzing the Reflections from Single Ommatidia in the Butterfly Compound Eye with Voronoi Diagrams.” *Journal of Neuroscience Methods* 131(1):195–203. doi: 10.1016/j.jneumeth.2003.08.011.
Walker, Simon M., Daniel A. Schwyn, Rajmund Mokso, Martina Wicklein, Tonya Müller, Michael Doube, Marco Stampanoni, Holger G. Krapp, and Graham K. Taylor. 2014. “In Vivo Time-Resolved Microtomography Reveals the Mechanics of the Blowfly Flight Motor.” *PLOS Biology* 12(3):e1001823. doi: 10.1371/journal.pbio.1001823.
Wardill, Trevor J., Samuel T. Fabian, Ann C. Pettigrew, Doekele G. Stavenga, Karin Nordström, and Paloma T. Gonzalez-Bellido. 2017. “A Novel Interception Strategy in a Miniature Robber Fly with Extreme Visual Acuity.” *Current Biology* 27(6):854–59. doi: 10.1016/j.cub.2017.01.050.
Warrant, Eric J. 1999. “Seeing Better at Night: Life Style, Eye Design and the Optimum Strategy of Spatial and Temporal Summation.” *Vision Research* 39(9):1611–30. doi: 10.1016/S0042-6989(98)00262-4.
Wehner, R., and I. Flatt. 1977. “Visual Fixation in Freely Flying Bees.” *Zeitschrift Für Naturforschung C* 32(5–6):469–472.

White, R. H. 2003. “The Retina of Manduca Sexta: Rhodopsin Expression, the Mosaic of Green-, Blue- and UV-Sensitive Photoreceptors, and Regional Specialization.” *Journal of Experimental Biology* 206(19):3337–48. doi: 10.1242/jeb.00571.

Woodman, Peter N., Amy M. Todd, and Brian E. Staveley. 2011. “Eyer: Automated Counting of Ommatidia Using Image Processing Techniques.” *Drosophila Information Service* 94:142.

Zhang, Zhi-Qiang. 2013. “Animal Biodiversity: An Update of Classification and Diversity in 2013. In : Zhang, Z.-Q. (Ed.) Animal Biodiversity: An Outline of Higher-Level Classification and Survey of Taxonomic Richness (Addenda 2013).” *Zootaxa* 3703(1):5–11. doi: 10.11646/zootaxa.3703.1.3.

Figures

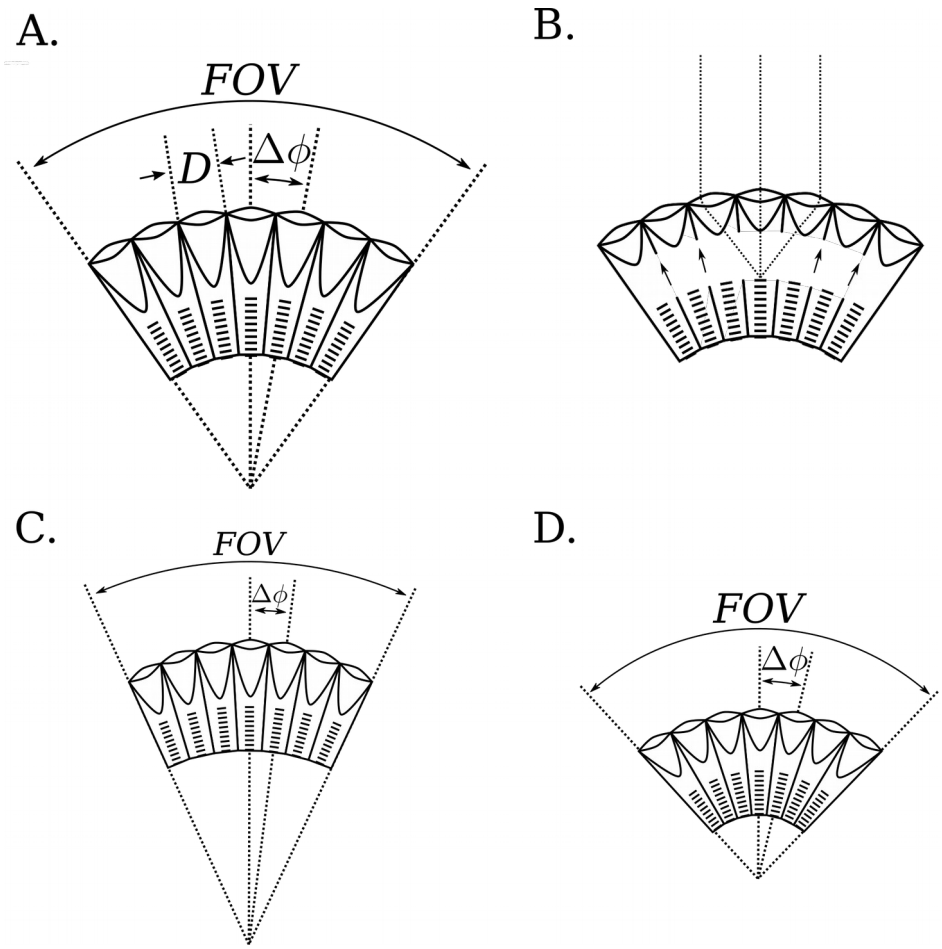

Figure 1: Diagrams of apposition and superposition eyes demonstrating the geometric tradeoffs between lens diameter (D), interommatidial angle (Δφ), and field of view (FOV) for spherical (A. and B.) and non-spherical eyes (C. and D.). **A.** In spherical apposition eyes, D directly determines sensitivity while Δφ inversely determines acuity. **B.** In superposition eyes, migrating pigment (indicated by the arrows) allows the ommatidia to share light, increasing the eye's sensitivity. As a result, these eyes must adhere to a spherical design. **C-D.** In non-spherical eyes, the intersection of ommatidial axes differs from the center of curvature, with ommatidial axes askew from the surface of the eye. Consequently, FOV and Δφ are not externally measurable and the effect of D on sensitivity is reduced by greater angles of skewness. **C.** When the distance to the intersection is greater than the radius of curvature, FOV and Δφ decrease, increasing average spatial acuity by directing more ommatidia over a smaller total angle. **D.** Inversely, when the distance to the intersection is less than the radius of curvature, FOV and Δφ increase, decreasing average spatial acuity by directing fewer ommatidia over a smaller total angle. In both cases, optical sensitivity is lost because skewness reduces the effective aperture of the ommatidia.

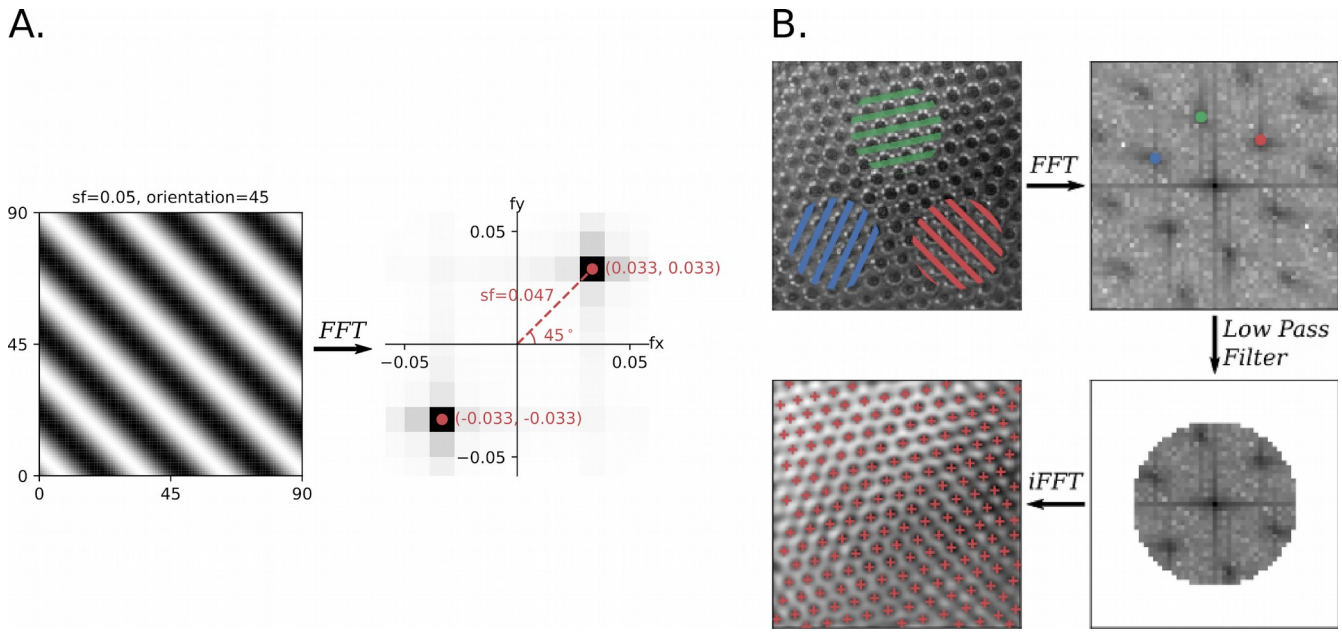

Figure 2: The ommatidia detecting algorithm (ODA) extracts periodic signals in a 2D image using the FFT. **A.** In the frequency domain of a 2D FFT, called the reciprocal space, gratings are represented by an x- and y-frequency. The polar coordinates represent visual properties of the corresponding grating. The radial distance is a grating's spatial frequency, with high frequencies farther from the origin. The polar angle is the grating's orientation , which is perpendicular to the grating's wavefront. Notice that the reciprocal space has local maxima (in red) approximately equal to the input grating parameters (polar angle=45° and radial distance=.047±.005). **B.** In a hexagonal lattice, there are three major axes (here in blue, green, and red). Each axis corresponds to a 2D spatial frequency (and it's negative), visible in the image's reciprocal space. The periodic nature of the axes results in harmonic frequencies. A low-pass filter returns a version of our original image primarily representing these three axes. The center of each ommatidium is found at the local maxima of the filtered image.

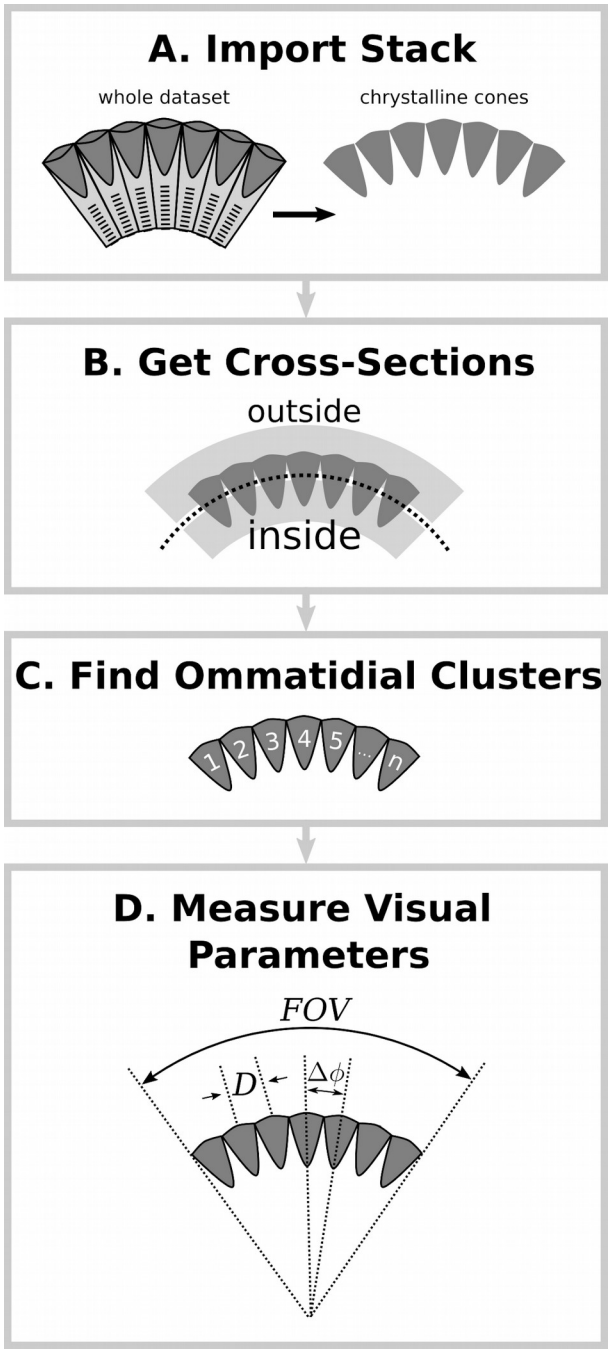

Figure 3: The µCT pipeline starts with an image stack, which may be pre-filtered and cleaned of unrelated structures. Then we filter the relevant density values and fit a surface to the coordinates, allowing us to split the points into two sets or cross sections, inside and outside the fitted surface. For each cross section, we generate spherically projected, rasterized images that are processed by the FFT method for locating ommatidia, yielding approximate centers for the ommatidia. With these centers, we can find the coordinate clusters corresponding to independent ommatidia and automatically measure eye parameters.

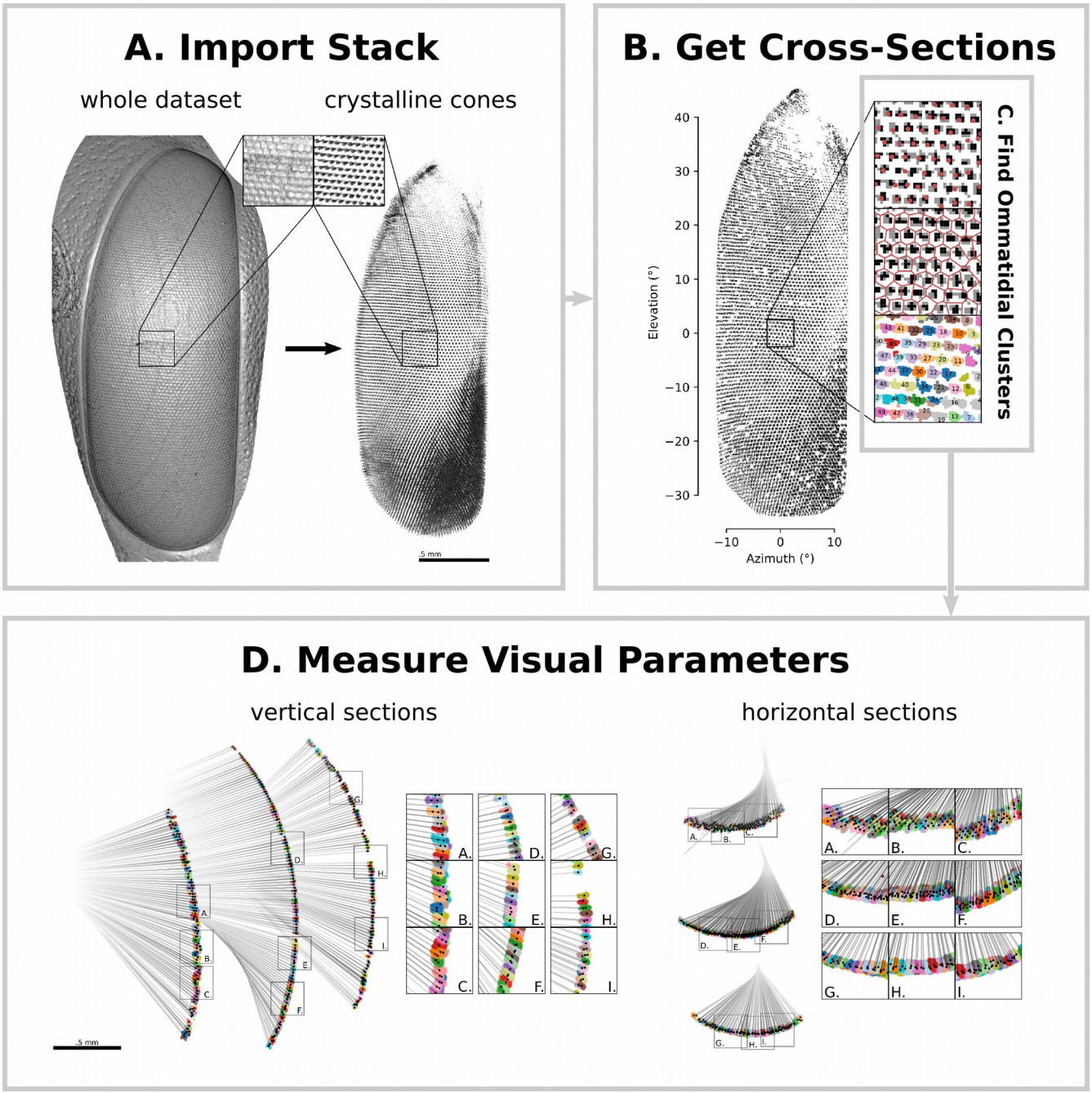

Figure 4: Checkpoints along the µCT pipeline for the bumblebee scan. **A. Import Stack**: The bumblebee µCT pipeline started with an image stack that we pre-filtered and manually cleaned of unrelated structures. **B. Get Cross-Sections:** A surface was fitted to the coordinates identifying a cross-section of points within 50% of the residuals. We generated a spherically projected, 2D histogram of the crystalline cone coordinates (in grayscale). **C. Find Ommatidial Clusters**: The inset zooms into stages of applying the ODA to label individual crystalline cones. The ODA locates the cluster centers (red dots in *top*), allowing us to partition the coordinates based on their distance to those centers (boundaries indicated by the red lines in *middle*). Then we apply the spectral clustering algorithm to all of the 3D coordinates using the ommatidia count (*bottom*), finding the clusters approximating the individual crystalline cones (each colored and labelled separately in *bottom*). **D. Measure Visual Parameters:** Ommatidial diameter corresponds to the average distance between clusters and their adjacent neighbors. Ommatidial count corresponds to the number of clusters. For

accounting for skewness in the ommatidial axes. The insets zoom into regions around the 25th, 50th, and 75th percentile ommatidia along the y-axis (*left*) and x-axis (*right*). Note: in **C** and **D** the different colors signify different crystalline cone clusters. In **D**, the black lines follow the ommatidial axes and the black dots indicate the cluster centroids.

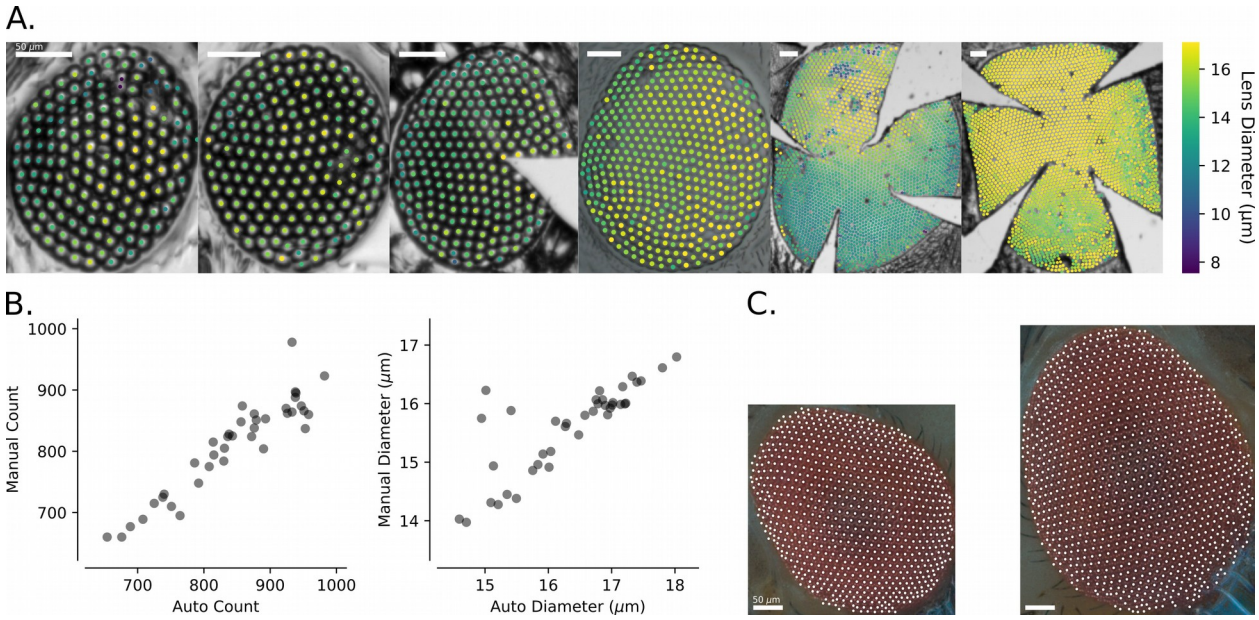

Figure 5: The ODA successfully approximated ommatidial counts and diameters when compared to manual measurements. **A.** When applied to 6 ant eye molds of 5 species ranging in overall size and lattice regularity, the automated counts were 97% and the diameters were 99% of those measured by hand. For each image, the program missed relatively few ommatidia and the lens diameter measurements were successful even when they varied substantially within an image (as in #5 from the left). Species from left to right: *Notoncus ectatommoides*, *Notoncus ectatommoides*, *Rhytidoponera inornata*, *Camponotus aeneopilosus*, *Myrmecia nigrocincta*, and *Myrmecia tarsata*. **B.** When applied to 39 microscope images of fruit fly eyes from the same species (*D. melanogaster*), the automated counts were 104% and the diameters were 105% of those measured by hand, with correlations of .93 and .82. **C.** Two example fruit fly eyes, one small and one large, with the automated ommatidia centers superimposed as white dots. Again, there were relatively low rates of false positives and negatives. Scale bars are 50µm.

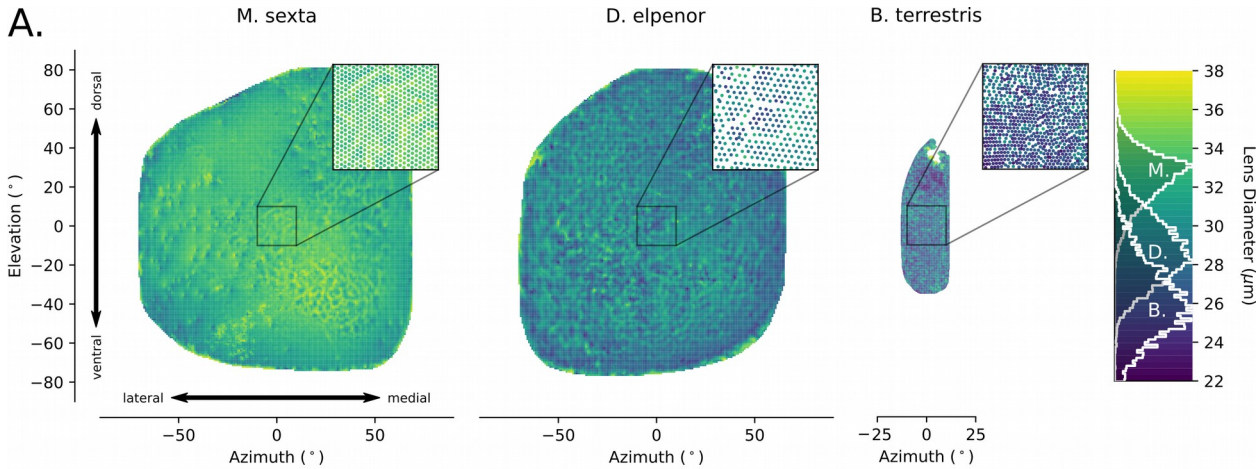

B.

Parameter	Species		
	M. sexta	*D. elpenor*	*B. terrestris*
Count	27756	13801	4765
Lens Diameter (μm)	32.5±1.5	28.8±1.9	26.1±2.1
Skewness (°)*	5.7±4.4	6.6±5.1	29.2±18.0
Adjusted Lens Diameter (μm)	32.2±1.6	28.4±1.9	22.1±3.7
Spherical IO Angle (°)*	0.88±.16	1.27±.35	0.74±.27
Anatomical IO Angle (°)*	0.94±.33	1.49±.74	2.60±1.94

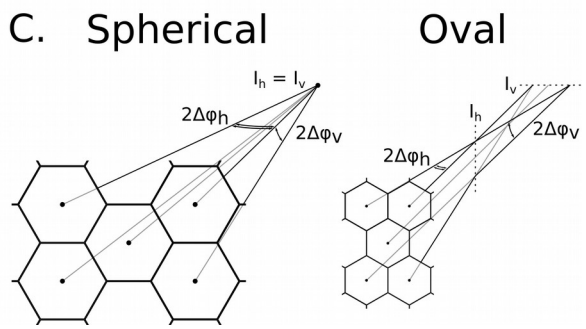

Figure 6: **A.** The MicroCT program allows us to map the visual fields of our three specimens. Using their spherical projection, we map the azimuth (along the lateral-medial axis) and elevation (along the ventral-dorsal axis) angles of ommatidia and represent lens diameter with color. The colorbar to the right indicates lens diameter, and shows diameter histograms for each species in white. Insets zoom in on a 20°x20° region in the center of each eye, showing ommatidial lattices in more detail. Note that the spherical projection of the bee eye underestimates its visual field and is missing a portion dorsally, as explained in the text. **B.** Optical parameters for the three species are presented as a table. Values are mean ± s.d except for angular measurements, indicated with an asterisk, which show median ± IQR. **C.** Adapted from (Stavenga 1979). Bee eyes are approximately oval, and, unlike spherical eyes, have different intersection points for horizontal (I_h) and vertical (I_v) ommatidial pairs corresponding to different IO angle components horizontally ($\Delta\varphi_h$) and vertically ($\Delta\varphi_v$). For oval eyes, the horizontal component of the IO angle of horizontal pairs (orientation=0°) is $2\Delta\varphi_h$ while the vertical component is ~0° and the horizontal component of diagonal pairs (orientation=±60°) is $\Delta\varphi_h$ while the vertical component is $\Delta\varphi_v$. Because the ommatidia form an approximately regular hexagonal lattice, $\Delta\varphi_v/\Delta\varphi_h = 1/\sqrt{3}$ for spherical eyes, and $\sqrt{3}$ for oval eyes.

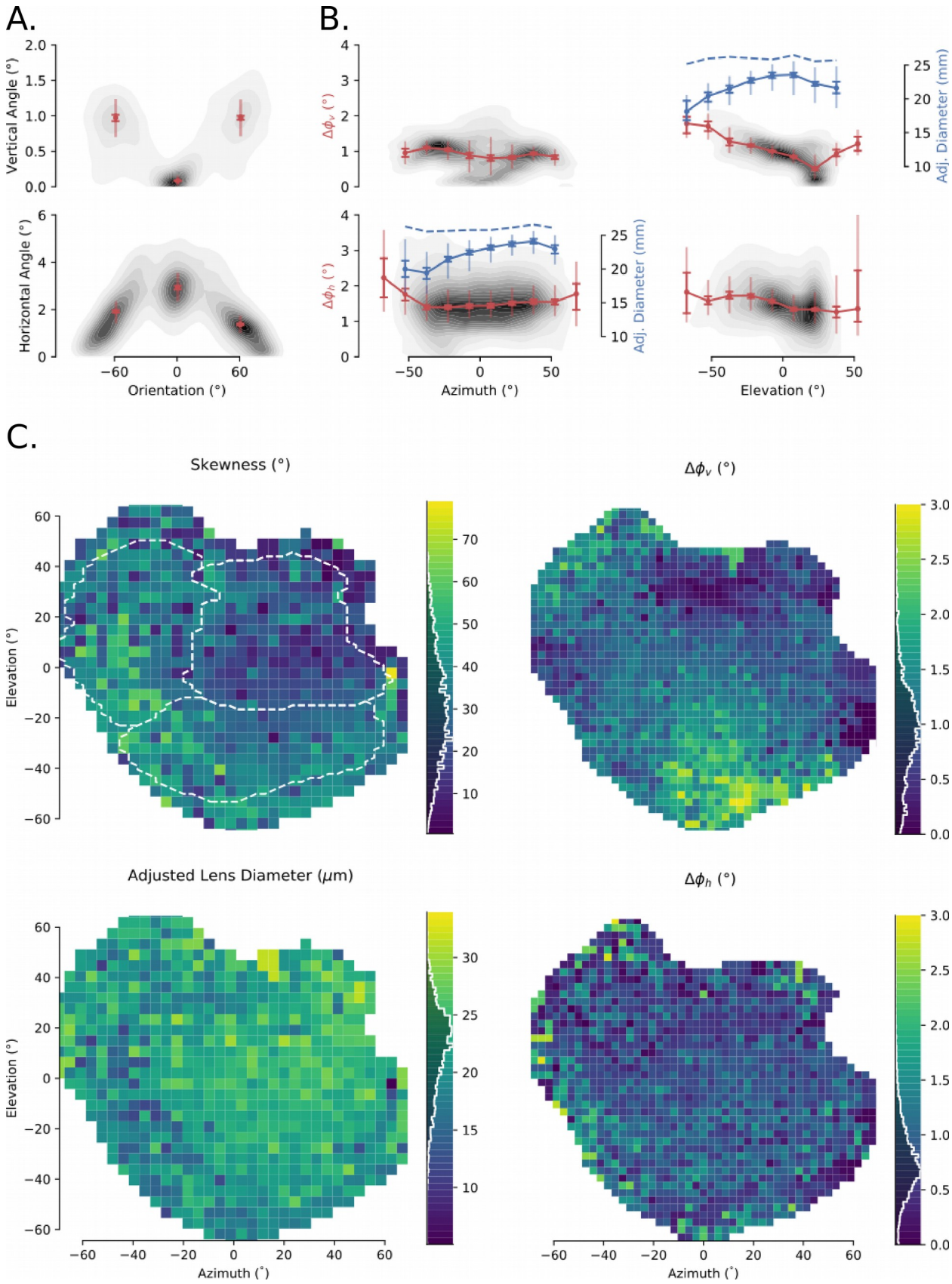
A.
B.
C.
Vertical Angle (°)
Horizontal Angle (°)
Orientation (°)
Azimuth (°)
Elevation (°)
Adj. Diameter (mm)
Skewness (°)
Adjusted Lens Diameter (μm)
Azimuth (°)
Elevation (°)

853

Figure 7: **A, B.** Grayscale heatmaps indicate kernel density estimation of the entire dataset and red lines indicate statistics about surrounding clusters: the longer, half opacity lines indicate IQR, tick marks indicate the 99% CI of the median using bootstrapping, and points (often overlapping with the tick marks) indicate the median. Solid blue lines, ticks, and points indicate the median and IQR of adjusted lens diameters in the same way as red lines, and correspond to inserted axes on the right. Dashed blue lines indicate the median absolute lens diameters also corresponding to the axes on the right. **A.** The vertical and horizontal subtended angles of ommatidial pairs with respect to their orientation fit well into the oval eye lattice from Figure 6C. The pair orientations form a trimodal distribution with means close to ±60° (diagonal pairs) and 0° (horizontal pairs). Medians, IQRs, and 99% C.I.s are plotted for each orientation ±15°. **B.** Using the lattice described in Figure 6C, we convert the horizontal and vertical subtended angles into the horizontal and vertical IO angle components ($\Delta\varphi_h$ and $\Delta\varphi_v$) and plot them with respect to their azimuth and elevation positions on the projected visual field. **C.** Skewness varies systematically across the eye influencing adjusted lens diameters and the horizontal and vertical IO angle components ($\Delta\varphi_h$ and $\Delta\varphi_v$). The position of each IO angle component is the average position of the two ommatidia per IO pair. Dashed white lines in the skewness map indicate three regions of generally different skewness: low skewness centrally and medially (top-right region; 19°) and moderate to high skewness ventrally (bottom region; 35°) and dorsal-laterally (bottom region; 37°).